The Astrophysical Journal, 874:130 (17pp), 2019 April 1 https://doi.org/10.3847/1538-4357/ab0b44

VEGAS: A VST Early-type GAlaxy Survey. IV. NGC 1533, IC 2038, and IC 2039: An Interacting Triplet in the Dorado Group

Arianna Cattapan[1], Marilena Spavone[1], Enrichetta Iodice[1], Roberto Rampazzo[2], Stefano Ciroi[3], Emma Ryan-Weber[4], Pietro Schipani[1], Massimo Capaccioli[5], Aniello Grado[1], Luca Limatola[1], Paola Mazzei[6], Enrico V. Held[2], and Antonietta Marino[6]

[1] INAF-Astronomical Observatory of Capodimonte, Salita Moiariello 16, I-80131, Naples, Italy; cattapan.arianna@gmail.com
[2] INAF-Astronomical Observatory of Padova, Vicolo dell'Osservatorio 8, I-36012, Asiago, Italy
[3] Department of Physics and Astronomy "G. Galilei"—University of Padova, Vicolo dell'Osservatorio 3, I-35122, Padova, Italy
[4] Centre for Astrophysics and Supercomputing, Swinburne University of Technology, Hawthorn, Victoria 3122, Australia
[5] University of Naples Federico II, C.U. Monte Sant'Angelo, via Cinthia, I-80126, Naples, Italy
[6] INAF-Astronomical Observatory of Padova, Vicolo dell'Osservatorio 5, I-35122, Padova, Italy
Received 2018 December 14; revised 2019 February 18; accepted 2019 February 26; published 2019 April 1

Abstract

This paper focuses on NGC 1533 and the pair IC 2038 and IC 2039 in Dorado a nearby, clumpy, still un-virialized group. We obtained their surface photometry from deep OmegaCAM@ESO-VST images in g and r bands. For NGC 1533, we map the surface brightness down to $\mu_g \simeq 30.11$ mag arcsec^{-2} and $\mu_r \simeq 28.87$ mag arcsec^{-2} and out to about 4 R_e. At such faint levels, the structure of NGC 1533 appears amazingly disturbed with clear structural asymmetry between inner and outer isophotes in the northeast direction. We detect new spiral arm-like tails in the outskirts, which might likely be the signature of a past interaction/merging event. Similarly, IC 2038 and IC 2039 show tails and distortions indicative of their ongoing interaction. Taking advantage of deep images, we are able to detect the optical counterpart to the H I gas. The analysis of the new deep data suggests that NGC 1533 had a complex history made of several interactions with low-mass satellites that generated the star-forming spiral-like structure in the inner regions and are shaping the stellar envelope. In addition, the VST observations also show that the two less luminous galaxies, IC 2038 and IC 2039, are probably interacting each other and IC 2038 could have also interacted with NGC 1533 in the past, which stripped away gas and stars from its outskirts. The new picture emerging from this study is that of an interacting triplet, where the brightest galaxy, NGC 1533, has ongoing mass assembly in the outskirts.

Key words: galaxies: elliptical and lenticular, cD – galaxies: evolution – galaxies: photometry

1. Introduction

Early-type galaxies (ETGs = Es+S0s) populating dense clusters represent the end product of a long evolution. Most early-type galaxies have exhausted their gas reservoir so that star formation quenched a long time ago. These galaxies represent the *template* of passively evolving ETGs (see, e.g., Bressan et al. 2006, for Virgo members), the so-called "red and dead" galaxy population (see, e.g., Boselli & Gavazzi 2014, and references therein). How and when the processes leading to the final quenching of star formation happened is still an open and widely debated question. Indeed, supporters of either a *gentle* or a *sudden* quenching process are found in the literature (see, e.g., Eales et al. 2017; Oemler et al. 2017; Weigel et al. 2017).

In less dense environments, a series of observations at different wavelengths have now shown that ETGs are, in general, "still alive" or at least "undead" with respect to their cluster counterparts. At optical wavelengths (Clemens et al. 2006 and references therein), analyzing Lick line-strength indices in central regions found that ETGs in the field are younger than those in environments typical of clusters. Young ETGs are those in which a recent episode of star formation occurred, *rejuvenating* their stellar population. Refining their analysis on a larger sample, Clemens et al. (2009) found that field ETGs are younger than their cluster counterparts by ~2 Gyr. At mid-infrared wavelengths, *Spitzer*-IRS (Houck et al. 2004; Werner et al. 2004) observations revealed the presence of polycyclic aromatic hydrocarbons (PAHs) in several nuclear regions of ETGs, in particular S0s (see, e.g., Kaneda et al. 2005; Panuzzo et al. 2011; Rampazzo et al. 2013, and references therein). The PAHs witness recent star formation activity. They arise from fresh carbonaceous material that is continuously released by a population of carbon stars, formed in a rejuvenation episode that occurred within the last few Gyr (Vega et al. 2010). The *Galaxy Evolution Explorer* (GALEX; Morrissey et al. 2007) via UV surveys as well as through deeper single target observations has contributed to many breakthroughs in revealing ongoing star formation in ETGs (Rampazzo et al. 2007; Jeong et al. 2009; Salim & Rich 2010; Marino et al. 2011a, 2011b). GALEX showed that star formation is not confined to the nuclear part but extends to the galaxy outskirts (e.g., in XUV disks Thilker 2008).

In this context, the study of the population of ETGs member of nearby, poor environments, like groups, is of overwhelming importance. In groups, we attend to both rejuvenation and quenching phenomena that are found only in the outskirts of clusters. Although in groups these mechanisms could differ from those acting in clusters (Boselli & Gavazzi 2014), because of the lower velocity dispersion of member galaxies, the importance of evolutionary mechanisms in groups is twofold. Groups contain more than 60% of the galaxies in the nearby universe and forge ETGs that will be accreted by clusters.

The history of galaxy transformation from active into passively evolving systems is written in the color–magnitude diagrams (CMd hereafter) of their galaxy populations. Particularly evident in optical versus UV CMd is the area inhabited by ETGs, i.e., the

red sequence, although they could be found also in the so-called *green valley*. The red sequence represents the final destination of galaxies, which, during their evolution, have passed from the blue cloud, inhabited by star-forming galaxies, via the green valley (Mazzei et al. 2014a, 2014b, 2018a, 2018b). CMds also tell us the evolutionary phase of the group. Young groups have a significant blue cloud at the expense of a depopulated red sequence. In evolved groups, the red sequence is well defined at basically all magnitudes of the galaxy population (Marino et al. 2016).

In recent years, a large effort was made to develop deep photometric surveys aimed at studying galaxy structures out to the regions of the stellar halos (e.g., Ferrarese et al. 2012; van Dokkum et al. 2014; Duc et al. 2015; Muñoz et al. 2015; Merritt et al. 2016; Trujillo & Fliri 2016; Mihos et al. 2017). In the last few years, the VST Early-type GAlaxy Survey[7] (VEGAS, Capaccioli et al. 2015) has occupied a pivotal role in the field by providing new insight on the faint regions of galaxies in all environments. VEGAS is a multiband u, g, r, and i imaging survey, able to map the surface brightness of galaxies down to the azimuthally averaged surface brightness $\mu_g \sim 30$ mag arcsec^{-2} and out to $\sim 10\,R_e$. Therefore, at these faint levels in surface brightness, with the VEGAS data, we are able to study the faintest regions of the galaxy outskirts and address the build-up history of the stellar halo by comparing the surface brightness profiles and the stellar mass fraction with the predictions of cosmological galaxy formation theories (Iodice et al. 2016, 2017a, 2017b; Spavone et al. 2017b, 2018). Moreover, thanks to the coverage of different morphological types, masses, and environments in VEGAS, we have started a study dedicated to the synoptic analysis of globular clusters (GCs) in different host galaxies (D'Abrusco et al. 2016; Cantiello et al. 2018). The VEGAS sample is made up of 58 ETGs brighter than $M_B = -21$ mag in different environments, including giant cD galaxies in the core of clusters, ETGs in groups of galaxies, and ETGs in low-density regions, in the local volume within $D \leqslant 54\,\mathrm{Mpc}/h$. In this paper we present the new deep data for one of the VEGAS targets: the Dorado group of galaxies.

1.1. The Dorado Group

The Dorado group, first identified by de Vaucouleurs (1975), has a backbone member structure that has been provided, more recently, by Firth et al. (2006). In that study, Dorado is described as a loose and clumpy group, un-virialized, centered at about $\alpha = 4^{\mathrm{h}}17^{\mathrm{m}}01\overset{\mathrm{s}}{.}8$ and $\delta = -55^{\mathrm{d}}42^{\mathrm{m}}46^{\mathrm{s}}$ (J2000), extending for several degrees ($\approx 10^\circ \times 10^\circ$) in projection. The distance of the Dorado group has a large uncertainty due to the membership definition: from 16.9 Mpc ($V_{\mathrm{hel}} = 1246 \pm 39$ km s^{-1}) given by Firth et al. (2006) to 21 Mpc by Brough et al. (2006). Following Firth et al. (2006), the velocity dispersion of the member galaxies (20 in total) is 222 ± 17 km s^{-1} with a crossing time of $0.126 \pm 0.006\ \mathrm{H}_0^{-1}$. The group CMd, shown in Figure 1, has a well-defined red sequence, a nearly depopulated blue cloud, and a set of member galaxies crossing the green valley. The brightest galaxies of the group are NGC 1549 (E0 − 1 NED[8]) and NGC 1553 (SA0$^0(r)$ NED), both showing a wide system of shells (Malin & Carter 1983). There are many galaxies showing interaction signatures suggesting that the group is going through a strongly evolving phase suggested also by the M_r versus (NUV-r) CMd (Cattapan et al. 2018; Rampazzo et al. 2018) described above. The group has a significant candidate dwarf galaxy population concentrated toward the group center detected by Carrasco et al. (2001). The dwarf galaxies' population would provide direct indication of the collapsed halo and the ratio giant versus dwarfs is larger when the group is dominated by ETGs (Tully 2015), as would be in the case of Dorado.

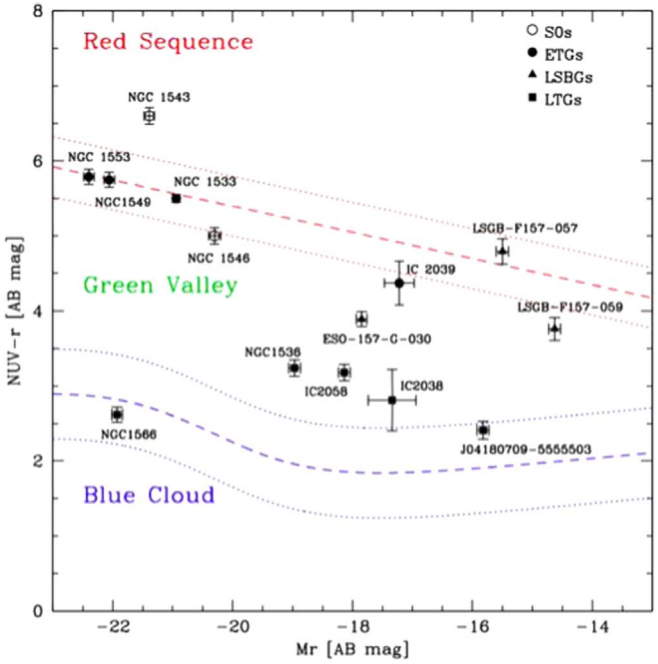

Figure 1. M_r vs. (NUV-r) color–magnitude diagram. The Wyder et al. (2007) fits (dashed lines), plus the error estimation (dotted lines), to the Red Sequence and Blue Cloud are shown. Empty circles mark lenticulars (S0s), full circles mark early-type galaxies (ETGs), full triangles mark low surface brightness galaxies (LSBGs), and full squares mark late-type galaxies (LTGs).

The subjects of this paper are NGC 1533, the fourth brightest galaxy member of Dorado, and the pair AM 0407-560, consisting of the two nearby fainter interacting galaxies, IC 2038 and IC 2039 (Arp & Madore 1987). The average radial velocity of the three galaxies is 771 ± 54 km s^{-1} (see Table 1), indicating that they belong to the same substructure in the group. In addition, the three galaxies are embedded in a cloud of H I identified with the HIPASS name J0409−56 (Ryan-Weber et al. 2003b) whose mass is $0.933 \times 10^9\,\mathcal{M}_\odot$ (using a distance of $D = 7.6$ Mpc; Ryan-Weber et al. 2003b). The shape and the velocity field of the H I cloud (Ryan-Weber et al. 2003a) support the view of a co-evolution of NGC 1533 and IC 2039 (Ryan-Weber et al. 2004; Bekki et al. 2005; Werk et al. 2010). The morphology of the lenticular NGC 1533 is complex as described by the Comerón et al. (2014) classification: it is a (RL)SB0° since it shows a complete, regular ring, a lens, and a bar, seen nearly face on. Both GALEX (Marino et al. 2011a) and *Swift*-UVOT observations (Rampazzo et al. 2017) have shown that NGC 1533 hosts ongoing star formation.

The paper is addressed to characterize, from accurate surface photometry, the structure of these galaxies up to the faintest surface brightness levels and to infer their possible interaction scenario. To this purpose we have obtained deep wide field exposures centered on NGC 1533 using the OmegaCAM@ESO-VLT in g and r SDSS filters.

[7] See http://www.na.astro.it/vegas/VEGAS/Welcome.html.

[8] NED Nasa/IPAC Extragalactic Database https://ned.ipac.caltech.edu.

Table 1
Basic Properties of Galaxy Sample

Galaxy	R.A. (h m s)	Decl. (° ′ ″)	Morph. Type	D (mag)	B_T (mag)	V_{hel} (km s^{-1})	σ (km s^{-1})	P.A. (deg NE)	ϵ
(1)	(2)	(3)	(4)	(5)	(6)	(7)	(8)	(9)	(10)
NGC 1533	04 09 51.8	−56 07 06	SB0$^-$	31.56 ± 0.14	11.79 ± 0.15	785 ± 8	177.5 ± 4.5	148.9	0.37
IC 2038	04 08 53.7	−55 59 22	Sd pec	31.42	15.42 ± 0.25	712 ± 52	⋯	155.2	0.74
IC 2039	04 09 02.4	−56 00 42	S0^0: pec	31.56	14.99 ± 0.14	817 ± 45	⋯	124.3	0.15

Note. Columns (2) and (3) are the J2000 coordinates; (4) morphological types are from RC3 (Third Reference Catalog of Bright Galaxies.); (5) the distance modulus from Tully et al. (2013) for NGC 1533, from Karachentsev et al. (2013) for IC 2038, and for IC 2039 we adopt the distance modulus of NGC 1533; (6) total apparent magnitude from HyperLeda (http://leda.univ-lyon1.fr); (7) radial heliocentric velocity 6df DR2 (Firth et al. 2006); (8) average value of central velocity dispersion from HyperLeda; mean position angle measured northeast (9) and ellipticity (10) of isophotes measured at $\mu_B = 25$ mag arcsec^{-2} HyperLeda.

Table 2
Observation Log for g and r Data

Filter (SDSS)	Date (yyyy mm dd)	R.A. (J2000) (deg)	Decl. (J2000) (deg)	T_{exp} (s)	Number Combined Frames	Seeing (FWHM) (arcsec)
(1)	(2)	(3)	(4)	(5)	(6)	(7)
g	2017 Oct 20/27	62.444	−56.101	7800	26	0.7893
r	2017 Oct 20/27	62.289	−56.114	4800	16	0.7852

Note. (1) Filters in the SDSS band; (2) dates of observations; (3) R.A. and decl. (4) of the center of the field of view; (5) total exposure time; (6) number of combined dithered frames; (7) median value of the seeing of the combined frames.

The plan of the paper is as follows. Section 2 reports observations and the reduction technique adopted. In Section 3 we present the performed isophotal analysis and in Section 4 we report the results obtained for each galaxy. In Section 5 we discuss results in the light of the current literature. Our conclusions are drawn in Section 6.

2. Observations and Data Reduction

The data we present in this work are part of the VEGAS Survey, which is based on the ESO-VLT Survey Telescope (VST) Guaranteed Time Observation (GTO) assigned at the Italian National Institute for Astrophysics (INAF). Our data set was obtained with VST+OmegaCAM in visitor mode (run ID 0100.B-0168(A)), in dark time, as summarized in Table 2. All observations were obtained by using the standard diagonal dithering for the scientific frame, in order to cover the gaps of the camera. Each science frame has an integration time of 300 s and we have obtained a total integration time of 2.2 hr in the g band and 1.3 hr in the r, in arcsec-level seeing conditions (see Table 2). Data were processed with the *VST-Tube pipeline*, described in detail by Grado et al. (2012) and Capaccioli et al. (2015, Appendix A).

Figure 2 shows the observed field of view in g band, centered on NGC 1533, and the color composite image using g (green channel) and r (red channel) band images from OmegaCAM@VST.

2.1. Sky Background Subtraction

For the final calibrated images obtained for the field around the brightest group member, NGC 1533, we have estimated and subtracted the sky background in each band using the IRAF[9] task IMSURFIT. This allows fitting the background contribution to the scientific images with a polynomial function. Thanks to the large field of view of OmegaCAM@VST, we estimated the background value by exploiting the region around NGC 1533, IC 2038, and IC 2039, where the contribution to the light of galaxies and background/foreground stars were masked. The best fit of the background contribution was achieved using a third-order Chebyshev polynomial function.

In the background-subtracted science frame, "residual fluctuations" of a few percent in flux could remain due to the flux variation of the background during the night. These are estimated on the final stacked image and set the accuracy of the background-subtraction step. To this aim, we extracted the azimuthally averaged intensity profile centered on NGC 1533 with IRAF task ELLIPSE, in each band, and we estimated the outermost radius R_{lim}, the distance from the galaxy's center where the galaxy's light blends into the average residual background level. This is the residual level, which persists after subtracting the background surface obtained by the polynomial fit, and it is very close to zero. We estimated the average sky fluctuation levels (Δ_{sky}) and the "amplitudes" of the distribution, i.e., the rms of the mean value at 1σ. We assume as the latest valuable science point in the surface brightness profile the point where flux $\geqslant\Delta_{sky}$. For NGC 1533, $R_{lim} \simeq 14.'91$ in the g band, while in the r band, $R_{lim} \simeq 13.'56$. Figure 3 shows an example of the above estimations in the g band. This method, which is well tested in the literature and also on the previous VEGAS data and analysis (see, e.g., Pohlen & Trujillo 2006; Iodice et al. 2014, 2016, 2017b, 2019; Capaccioli et al. 2015; Spavone et al. 2017b, 2018) allows measurement of any residual fluctuations in the background-subtracted image and then takes them into account in the luminosity and surface brightness measurements and related errors.

3. Surface Photometry: Isophotal Analysis and Light Distribution

The isophotal analysis is performed with the ELLIPSE task in IRAF (Jedrzejewski 1987) up to the limiting radius on the final stacked images in each band. ELLIPSE provides both the

[9] Image reduction and analysis facility http://iraf.noao.edu.

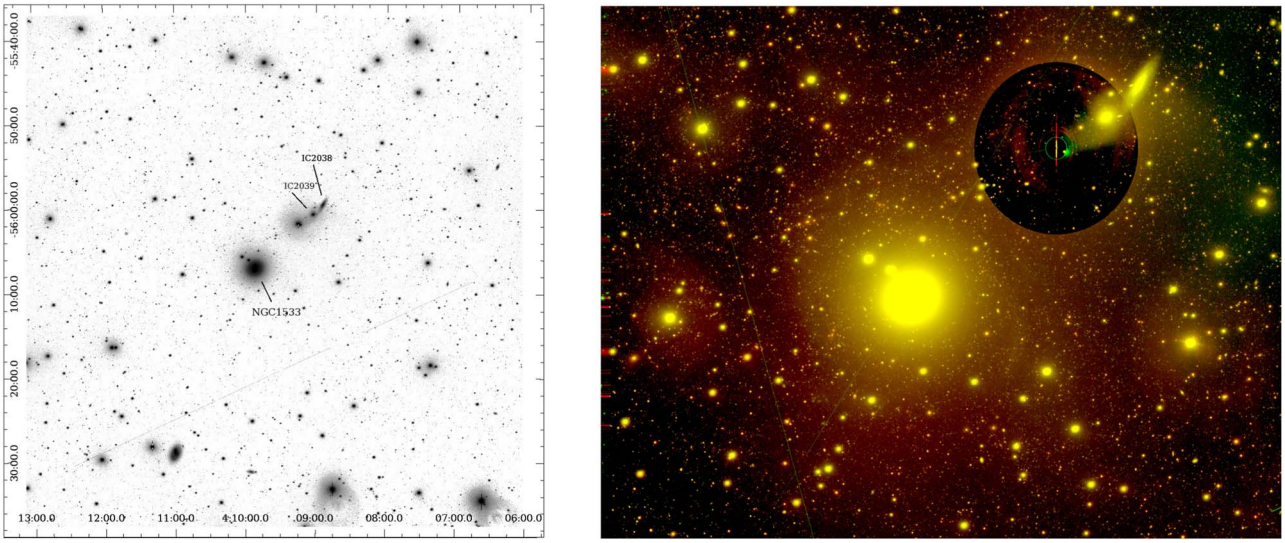

Figure 2. Left panel: OmegaCAM@VST g band observed field of view, centered on NGC 1533. The image size is $\sim 1^\circ \times 1^\circ$. Right panel: color composite image, $\sim 24' \times 19'$, of NGC 1533, IC 2038 and IC 2039. North is at the top, east is on the left.

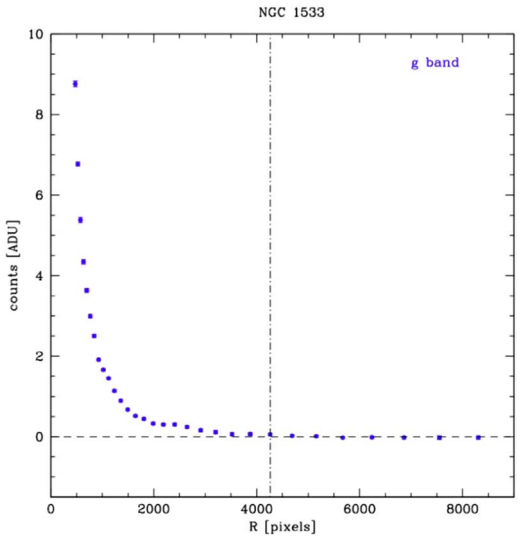

Figure 3. Azimuthally averaged intensity profile in counts as a function of the semimajor axis of ELLIPSE for g images of NGC 1533. The vertical dash–dotted line indicates the outermost radius; the horizontal dashed line represents the mean residual background fluctuations.

geometrical parameters and the azimuthally averaged light distribution profiles. The error on the surface brightness accounts for the errors on the residual background (Section 2.1) and the zero-point errors $ZP_g = 24.5036 \pm 0.0018$ and $ZP_r = 24.3820 \pm 0.0012$ (Capaccioli et al. 2015). For each galaxy, i.e., for NGC 1533 and for the two companion galaxies IC 2038 and IC 2039, we have derived the azimuthally averaged surface brightness profiles and the shape parameters of the isophotes: the ellipticity (ϵ), the position angle (P.A.), and the a_4 and b_4 (see Jedrzejewski 1987). In the outer parts of galaxies, for NGC 1533 at radii larger than $\sim 5'$, the signal-to-noise ratio is very low because the galaxy light begins to become comparable to the background residual fluctuations, therefore all the geometrical parameters are affected by strong fluctuations and large errors.

The results are described in Section 4 and a detailed analysis based on the geometrical parameters is reported in the Appendix. The total magnitudes and the effective radii are estimated from the galaxy growth curve. The absolute magnitudes and the total luminosity in solar units[10] come from previous data and from considering the galaxy distances (see Table 1). For the three galaxies, these parameters are listed in Table 3.

We derived the azimuthally averaged color profiles and, from images, the two-dimensional color maps. The mean $g - r$ values, reported in Tables 4 and 5, are calculated up to the radii where the errors are less than $\sim$0.1–0.2 mag. Finally, using stellar population synthesis models (Ricciardelli et al. 2012; Vazdekis et al. 2012) with $\log Z/Z_\odot = 0$ and a Kroupa initial mass function, and considering the average color that provides a stellar mass-to-light ratio ($\mathcal{M}/L$) in the r SDSS band (Iodice et al. 2017b), we estimate the total stellar mass (see Tables 4 and 5).

3.1. The Effect of Point-spread Function (PSF) on the Light Distribution

According to de Jong (2008), La Barbera et al. (2012), and Trujillo & Fliri (2016, and references therein), it is important, especially for the brightest cluster galaxies (BCGs, hereafter), to account for the effect of the contamination from the galaxies' bright cores and scattered light. This is done by mapping the PSF out to a comparable radial distance of the galaxy stellar halo. We use the extended PSF derived for VST images by Capaccioli et al. (2015, Appendix B). The deconvolution was successfully applied at the bright galaxies in the VEGAS survey by Spavone et al. (2017b) and it is based on the the Lucy–Richardson algorithm (Richardson 1972; Lucy 1974). A full description of the deconvolution method used for VST data will be presented in a forthcoming paper by M. Spavone et al. (2019, in preparation). The deconvolved azimuthally averaged surface brightness g and r-band profiles for NGC 1533 are shown in Figure 4. As expected (see also de Jong 2008), in the seeing-dominated regions, $R < 1''$, the surface brightness profiles are brighter, of about 0.7–0.75 mag arcsec^{-2} for both

[10] Absolute magnitudes of the Sun are reported in the following website: http://mips.as.arizona.edu/~cnaw/sun.html.

Table 3
Main Results for NGC 1533, IC 2038, and IC 2039

Galaxy	$m_{\mathrm{tot},g}$ (mag)	$m_{\mathrm{tot},r}$ (mag)	$R_{e,g}$ (arcsec)	$R_{e,r}$ (arcsec)	M_g (mag)	M_r (mag)	L_g ($L_\odot$)	L_r ($L_\odot$)
(1)	(2)	(3)	(4)	(5)	(6)	(7)	(8)	(9)
NGC 1533	10.48 ± 0.05	9.60 ± 0.05	64.17 ± 0.16	78.20 ± 0.41	-21.08 ± 0.34	-21.96 ± 0.34	2.99×10^{10}	4.40×10^{10}
IC 2038	14.29 ± 0.08	13.94 ± 0.05	⋯	⋯	-17.13 ± 0.08	-17.48 ± 0.05	7.87×10^{8}	7.11×10^{8}
IC 2039	14.41 ± 0.05	13.84 ± 0.05	⋯	⋯	-17.15 ± 0.05	-17.72 ± 0.05	8.01×10^{8}	8.86×10^{8}

Note. (1) Galaxy name. Total magnitude in g, (2), and r, (3), bands. Effective radius in g, (4), and r, (5), bands. Absolute magnitudes in g, (6), and r, (7), bands. Total luminosity in solar units in g, (8), and r, (9), bands.

bands. In the outer regions, for $R \geqslant 1.5$ arcmin, the profiles are steeper.

4. Results

OmegaCAM@VST deep photometry allows us to reach the surface brightness limits of $\mu_g = 30.11 \pm 1.2$ mag arcsec^{-2} and $\mu_r = 28.87 \pm 0.6$ mag arcsec^{-2} at $R = 4\farcm75$ ($\sim$16.19 kpc) for NGC 1533 (Figure 5, left panel). The VST image in the g-band surface brightness levels is shown in Figure 6.

In the following subsections we describe the results obtained by mapping the light and color distributions beyond the unprecedented limits. In order to reduce the contamination of the light coming from the bright star CD−56 854, ($\alpha_{J2000} = 4^{\mathrm{h}}9^{\mathrm{m}}15\overset{\mathrm{s}}{.}03$ and $\delta_{J2000} = -56^{\mathrm{d}}01^{\mathrm{m}}48\overset{\mathrm{s}}{.}45$), it has been modeled by using a Gaussian function and subtracted from both bands images; all photometric analysis takes into this account, as shown in Figures 2 and 6.

4.1. The Faint Features in NGC 1533, IC 2038, and IC 2039 Outskirts

The deep images obtained for NGC 1533 with OmegaCAM@VST allow us to map the light distribution out to the galaxy outskirts and detect new faint features in these regions. In the g band, the outskirts of NGC 1533 appear asymmetric, i.e., light is elongated on the northeast side. We found three faint $\mu_g \geqslant 28$–30 mag arcsec^{-2} spiral-like tails in the north–northwest outskirt of the galaxy (see Figure 6). In addition, we detected an extended ($\sim 5'$) arc-like structure with $\mu_g \sim 28$–30 mag arcsec^{-2} protruding from the two interacting galaxies, IC 2038 and IC 2039, on the west side. The tails in the outskirts of NGC 1533 are still evident in r-band image, while the faint arc-like structure on the west does not appear in this band. This would be hint of a bluer color for this structure or, alternatively, it is comparable to the background level so it was accounted for in the polynomial fit of the sky fluctuations.

Comparing the previous works on NGC 1533 (e.g., Ryan-Weber et al. 2003b, 2004; Werk et al. 2008) and thanks to the deep VST image, we are able to associate the optical counterpart to the H I gas. Figure 6 shows the overlap of the deep VST g-band image in surface brightness levels and the H I contours levels (where they are at column densities of 2.5, 2.8, 3.1, 3.5, 3.9, 4.2 $\times 10^{20}$ atoms cm^{-2}). As it is anticipated by Bekki's simulations, an N-body/SPH numerical simulation, using the Fall & Efstathiou (1980) model, of a minor, unequal-mass merger (Ryan-Weber et al. 2003b), the surface brightness of stellar remnants is down to $\sim$26–29 mag arcsec^{-2}. At these levels, $\mu_g \gtrsim 28.5$ mag arcsec^{-2}, we are able to trace the regions of the stellar envelope, which appears asymmetric and more elongated toward NE (in correspondence of Tail3). We find an overlap between the new faint features detected from the deep VST images and the H I distribution. It seems that most of the H I is within the stellar envelope of the galaxy on the region where it appears more elongated, so the light overdensity corresponds to the H I overdensity. The H I on west side is also concentrated on the two spiral-like tails (Tail1 and Tail2) in the stellar envelope on the galaxy.

4.2. Light and Color Distribution

NGC 1533—From the isophote fit, we made the two-dimensional model of the galaxy in the g band by using the IRAF task BMODEL and we derived the residual image, shown in Figure 7. Residuals clearly revealed an optical previously undetected arm-like structure, which is brighter in the inner regions, $30'' \leqslant R \leqslant 60''$, but still evident at larger radii, where the faint tails on west side (see Figure 6) also stand out. The same structure is also detected in the 2D $g - r$ color map (see Figure 8, bottom panel). The spiral-like pattern resemble a spiral disk where redder arms ($g - r \sim 0.8$ mag) are interloped by bluer arms ($g - r \sim 0.72$–0.78 mag) made of dust and young stars.

The azimuthally averaged surface brightness profiles in the g and r bands are shown in Figure 5 (left panel). From a visual inspection, the galaxy is made by the inner luminous bulge, followed by a lens and bar plateau, and the outer ring lens, disk, and stellar envelope component. The multi-component fit, to set the scale of the most luminous components dominating the light distribution, is performed and described in Section 4.3.

The mean color value, estimated from the azimuthally averaged extinction-corrected (Schlafly & Finkbeiner 2011) and PSF-deconvolved $g - r$ color profile (Figure 8, top panel), up to $\sim 5'$, is 0.77 ± 0.05 mag (see also Table 4).

The effect of the PSF wings at large radial distances can alter the color profile of galaxies, showing the so-called *red halo phenomenon* (Michard 2002; Zackrisson et al. 2006; La Barbera et al. 2012, and references therein). It depends more on the observational bands: the redder the band, the greater the red gradient in the galaxy outskirts color profile. Figure 8 (top panel) shows the color profile of NGC 1533 before and after the PSF deconvolution. It is clear that in the outer regions, $R > 1'$, the mean color changes from $\sim$0.95 mag to $\sim$0.46 mag.

Finally, for face-on and round galaxies, as NGC 1533, the PSF deconvolution does not modify the geometrical parameters of the outer isophotes because the PSF effects are larger for bright, smaller, and edge-on galaxies (Michard 2002; de Jong 2008).

Using the growth curve, we derived the total magnitudes and effective radii (R_e) and hence the absolute magnitudes and the total luminosity in solar units are estimated in the g and r

Table 4
Best Fitting Structural Parameters for a Three-component Fit of NGC 1533

Filter	r_{e1} (arcsec)	n_1	μ_{e1} (mag arcsec^{-2})	$m_{\rm tot,1}$ (mag)	r_{e2} (arcsec)	n_2	μ_{e2} (mag arcsec^{-2})	$m_{\rm tot,2}$ (mag)	r_0 (arcsec)	μ_0 (mag arcsec^{-2})	$m_{\rm tot,3}$ (mag)	$f_{h,T}$	$g-r$ (mag)	$(M/L)_r$ ($\mathcal{M}_\odot/L_\odot$)	$\mathcal{M}^*_{\rm tot}$ ($\mathcal{M}_\odot$)	$\mathcal{M}^*_{\rm tot\ acc}$ ($\mathcal{M}_\odot$)
(1)	(2)	(3)	(4)	(5)	(2)	(3)	(4)	(5)	(2)	(4)	(5)	(6)	(7)	(8)	(9)	(10)
g	5.04 ± 0.06	2.34 ± 0.68	18.88 ± 0.53	11.98	39.48 ± 8.97	1.20 ± 0.16	21.97 ± 0.88	10.60	109.86 ± 1.5	25.58 ± 0.01	13.38	79%	0.77 ± 0.05	2.88	1.27×10^{11}	0.99×10^{11}
r	5.00 ± 0.40	2.29 ± 0.10	18.05 ± 0.21	11.17	39.02 ± 4.22	1.20 ± 0.10	21.19 ± 0.01	9.85	57.92 ± 0.24	23.71 ± 0.64	12.9	78%	...	...	...	...

Note. (1) Filters. Best-fit parameters of the PSF-deconvolved light profile decomposition: (2) effective and scald radius; (3) Sérsic index, (4) effective and central surface brightness of the different components, and (5) total magnitude of the individual component. (6) Total accreted mass fraction derived from our fit. (7) Averaged extinction-corrected and PSF-deconvolved $g-r$ color value and relative mass-to-light ratio in r band (8). Total stellar mass (9) and total accreted stellar mass fraction derived from the three-component fits (10) in r band.

Table 5
Best Fitting Structural Parameters for a Two-component Fit

Galaxy	Filter	r_{e1} (arcsec)	n_1	μ_{e1} (mag arcsec^{-2})	$m_{\rm tot,1}$ (mag)	r_0 (arcsec)	μ_0 (mag arcsec^{-2})	$m_{\rm tot,3}$ (mag)	$f_{h,T}$	$g-r$ (mag)	$(M/L)_r$ ($\mathcal{M}_\odot/L_\odot$)	$\mathcal{M}^*_{\rm tot}$ ($\mathcal{M}_\odot$)	$\mathcal{M}^*_{\rm tot\ acc}$ ($\mathcal{M}_\odot$)
	(1)	(2)	(3)	(4)	(5)	(2)	(4)	(5)	(6)	(7)	(8)	(9)	(10)
IC 2038	g	18.89 ± 1.10	1.01 ± 0.09	23.15 ± 0.54	13.38	26.47 ± 4.79	22.39 ± 0.13	13.28	52%	0.41 ± 0.08	0.62	4.41×10^8	2.0×10^8
	r	19.47 ± 0.39	0.99 ± 0.02	22.40 ± 0.09	12.57	42.11 ± 0.45	22.88 ± 0.10	12.76	45%	⋯	⋯	⋯	⋯
IC 2039	g	8.55 ± 0.73	1.61 ± 0.11	22.11 ± 0.13	14.06	89.87 ± 19	24.36 ± 0.16	12.6	79%	0.71 ± 0.20	1.53	1.36×10^9	1.18×10^9
	r	10.18 ± 0.24	1.66 ± 0.70	21.89 ± 0.61	13.46	132.26 ± 19.50	24.05 ± 0.08	11.45	86%	⋯	⋯	⋯	⋯

Note. (1) Filters. Best-fit parameters of the light profile decomposition: (2) effective and scale radius; (3) Sérsic index, (4) effective and central surface brightness of the different components, and (5) total magnitude of the individual component. (6) Total accreted mass fraction derived from our fit. (7) Averaged extinction-corrected $g-r$ color value and relative mass-to-light ratio in r band (8). Total stellar mass (9) and total accreted stellar mass fraction derived from the three-component fits (10) in r band.

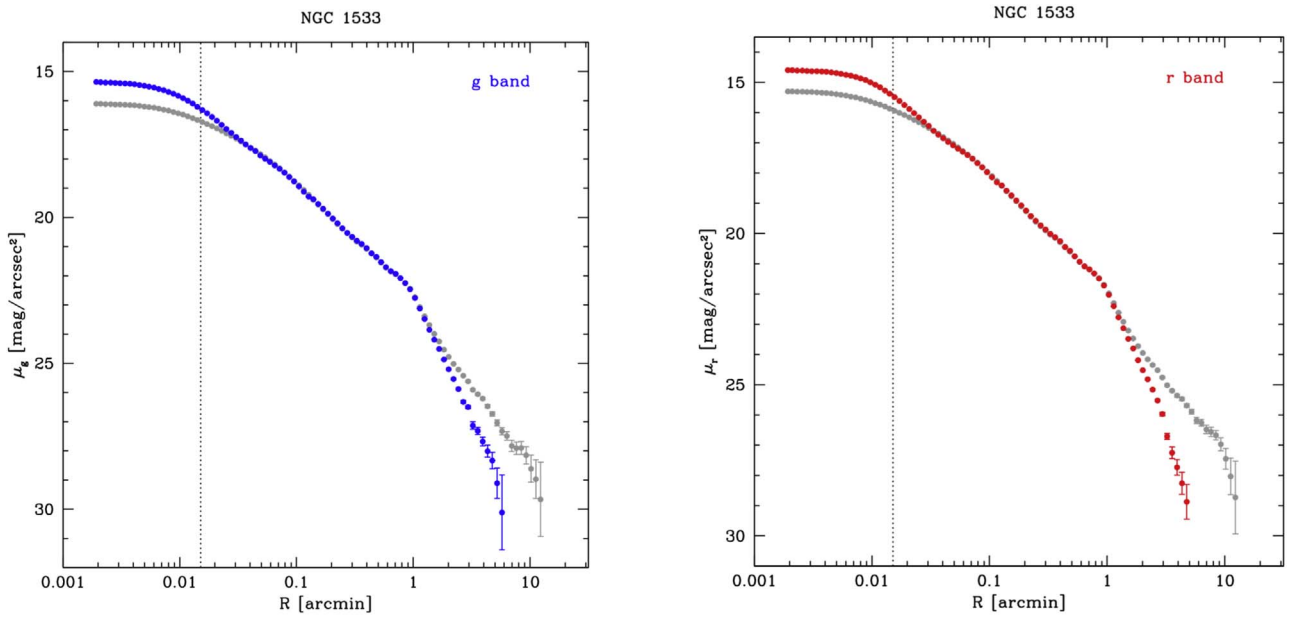

Figure 4. *g*-band (left panel) and *r*-band (right panel) azimuthally averaged surface brightness profiles as a function of the logarithmic isophote semimajor axis. The gray dots correspond to the original profiles, the blue (*g* band) and red (*r* band) dots indicate the PSF-deconvolved profiles.

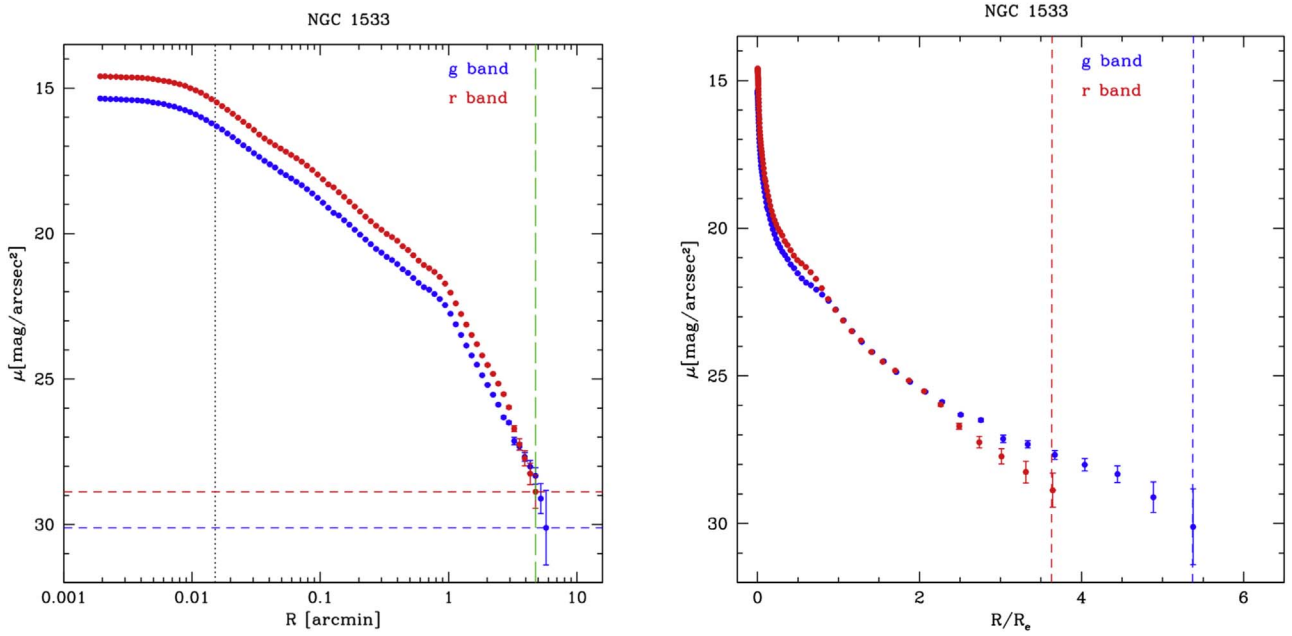

Figure 5. Left panel: azimuthally averaged and PSF-deconvolved surface brightness profile as a function of the logarithmic isophote semimajor axis; the black dotted line delimits the seeing-dominated region. The red and blue dashed lines represent the faint surface brightness reached: $\mu_g = 30.11$ mag arcsec^{-2} and $\mu_r = 28.87$ mag arcsec^{-2}; the green dashed line indicates relative radius $R = 4\farcm75$. Right panel: averaged and PSF-deconvolved surface brightness profile as a function of the isophote semimajor axis normalized to the effective radius. The red and blue dashed lines indicate the R/R_e distances joined.

bands, respectively (see Table 3). The effective radii in the *g* and *r* bands are $R_e \sim 5.93$ kpc and $R_e \sim 7.23$ kpc, respectively. Therefore, the surface brightness profiles extend out to $\sim 5\,R_e$ and $\sim 4\,R_e$, respectively (see Figure 5, right panel).

IC 2038 and IC 2039—The azimuthally averaged surface brightness profiles derived for IC 2038 and IC 2039 are shown in Figures 9 (top panel) and 10 (top panel), respectively. Figure 9 (bottom panel) shows the azimuthally averaged color profile of IC 2038, Figure 10 (bottom panel) of IC 2039 (see also Table 5). The mean color value of IC 2038 is $g - r = 0.41 \pm 0.08$ mag, which is consistent with the typical colors observed for late-type galaxies (Strateva et al. 2001). It shows a consistent decrease, of about 0.04 mag out to $R \sim 4\farcs1$, in the region where spiral arms dominate the galaxy structure. IC 2039 is redder, with $g - r = 0.71 \pm 0.20$ mag (see also Table 5), which is comparable with the typical colors observed for early-type galaxies (La Barbera et al. 2012). The color profile shows a blue dip in the inner regions, where $0.38 \leqslant g - r \leqslant 0.61$ mag for $0\farcs9 \leqslant R \leqslant 3\farcs2$. At larger radii, the color profile has a scattered trend in a wide range of values, $g - r \sim 0.6$–1.1 mag out to $\simeq 26''$.

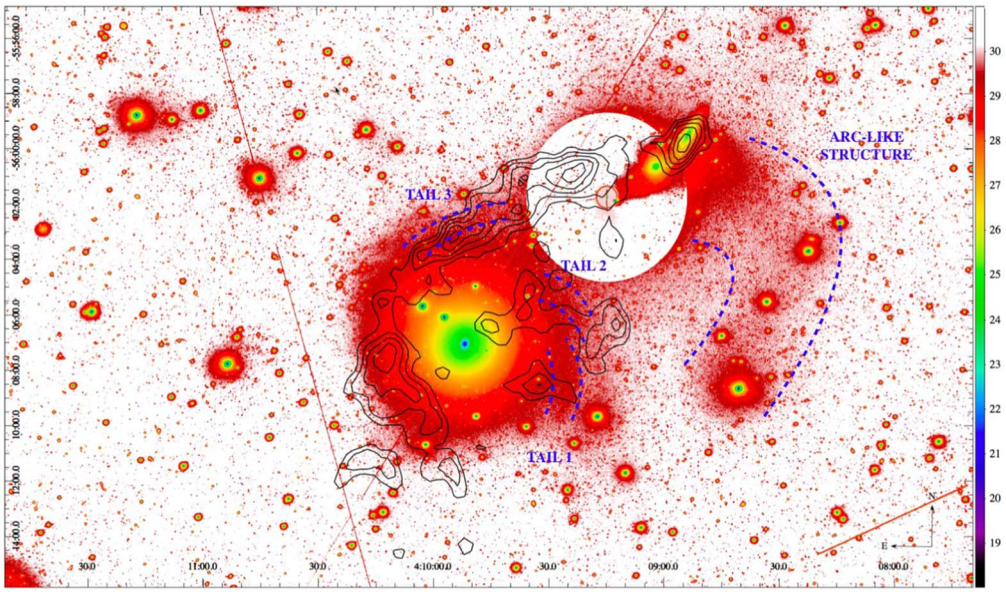

Figure 6. Surface brightness levels in g band of the NGC 1533 system, with the H I map from the Australia Telescope Compact Array (ATCA) superimposed (black contours). The contours are 2.5, 2.8, 3.1, 3.5, 3.9, 4.2 $\times$ 10^{20} atoms cm^{-2} and have a resolution of $\sim 1'$ (Ryan-Weber et al. 2003b). The spiral-like tails have a central distance of $229''.27$, $237''.02$ and $220''.34$ ($\sim$21.19, 21.90, 20.36 kpc), respectively, for Tail1, Tail2, and Tail3; the arc-like structure is extended for $\sim 5'$ and has a mean central distance of $\sim 9'$ ($\sim$49.90 kpc).

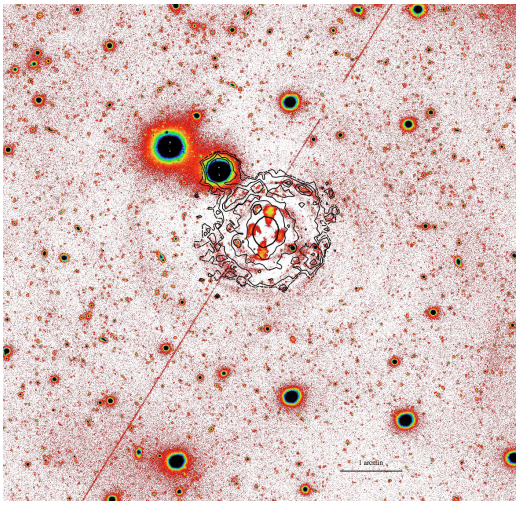

Figure 7. Residual image ($8'.30 \times 7'.95$) from VST g band of NGC 1533 inner region with the contours (levels are 25.26 (bold), 25.85, 26.10, 26.29, 26.41 (dashed) mag arcsec^{-2}) obtained from the $W2$ filter image *Swift*-UVOT (Rampazzo et al. 2017).

4.3. Multi-component Fit of the Light Distribution

In order to define the scales of the main components that dominate the light distribution in NGC 1533, we performed a multi-component fit to reproduce the surface brightness profile, as done for the BCGs at the center of the groups and clusters (Seigar et al. 2007; Donzelli et al. 2011; Arnaboldi et al. 2012; Cooper et al. 2013; Huang et al. 2013; Cooper et al. 2015; Iodice et al. 2016, 2019; Rodríguez et al. 2016; Spavone et al. 2017b, 2018). BCGs consist of at least two components, the bright spheroidal body and the outer and very extended, moderately flattened, stellar envelope.

Even if the isophotal analysis has shown that the inner structure of NGC 1533 is quite complex, including a bar and a lens, we adopted a simple model that should reproduce the most luminous components of the galaxy. Therefore, the residuals would point out the main subcomponents hidden in the light distribution.

As a starting point, we performed a least-squares fits using a Levenberg–Marquardt algorithm (Seigar et al. 2007; Spavone et al. 2017b) of the azimuthally averaged surface brightness profile g band. Our model is made up by a composition of Sérsic power law (Sérsic 1963), $\mu(R) = \mu_e + k(n)\left[\left(\frac{R}{r_e}\right)^{1/n} - 1\right]$, where R is the galactocentric radius, r_e the effective radius, μ_e the surface brightness at the effective radius, $k(n) = 2.17n - 0.355$ (Caon et al. 1993), and exponential law (Freeman 1970), $\mu(R) = \mu_0 + 1.086 \times \frac{R}{r_h}$, where R is the galactocentric radius, r_h the exponential scale length, and μ_0 the central surface brightness (see Tables 4, 5 and Figure 14). The total magnitude obtained from the fit is $\sim$0.5 mag brighter than that measured from the growth curve. Such a difference is due to the exclusion of the central seeing-dominated regions ($R \leqslant 0''.79$) from the fit.

Considering the state-of-art of studies on the multi-component fit of the light distribution (see, e.g., Spavone et al. 2017a, 2018, and references therein) it is possible to derive the relative contribution of the accreted component with respect to the total galaxy light, $f_{h,T}$, and the total accreted mass fraction (see Tables 4 and 5).

The structural parameters obtained by the one-dimensional fit (see Tables 4 and 5) are used as starting guesses for the two-dimensional fit, performed by using GALFIT.[11] In order to improve the quality of the resulting model and residual image, we have added in the input file the mask of all the bright sources and background/foreground objects and the mean value of the residual background fluctuations.

[11] GALFIT is a data analysis algorithm that fits 2D analytic functions of galaxies and point sources directly to digital images. A detailed description of the GALFIT technique can be found in Peng et al. (2002), with new features found in Peng et al. (2010, https://users.obs.carnegiescience.edu/peng/work/galfit/galfit.html).

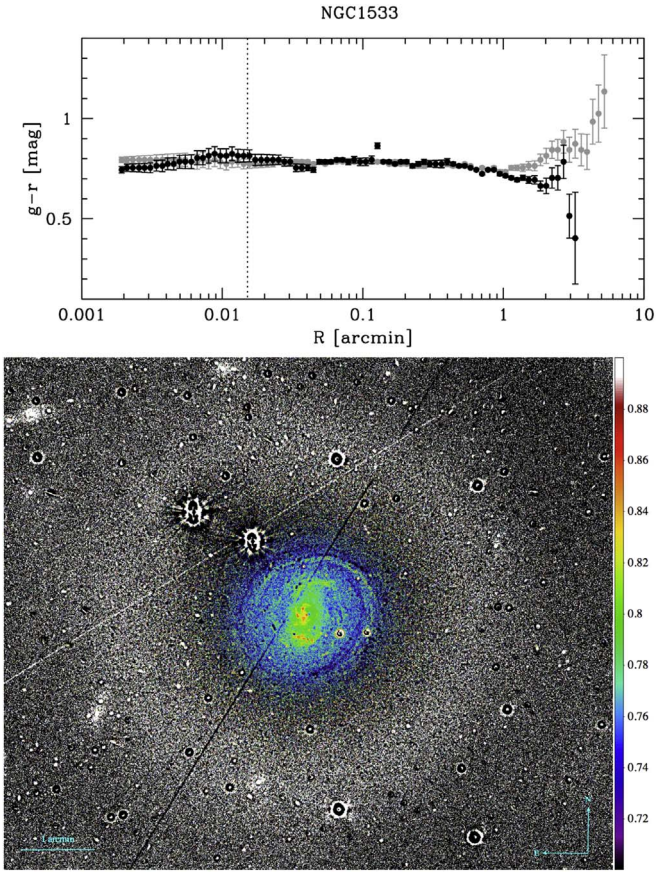

Figure 8. Top panel: azimuthally averaged extinction-corrected color profile as a function of the logarithmic isophote semimajor axis; original profile (gray dots) and deconvolved profile (black dots). The black dotted line delimits the seeing-dominated region. Bottom panel: 2D color map centered in NGC 1533 made using the deconvolved images.

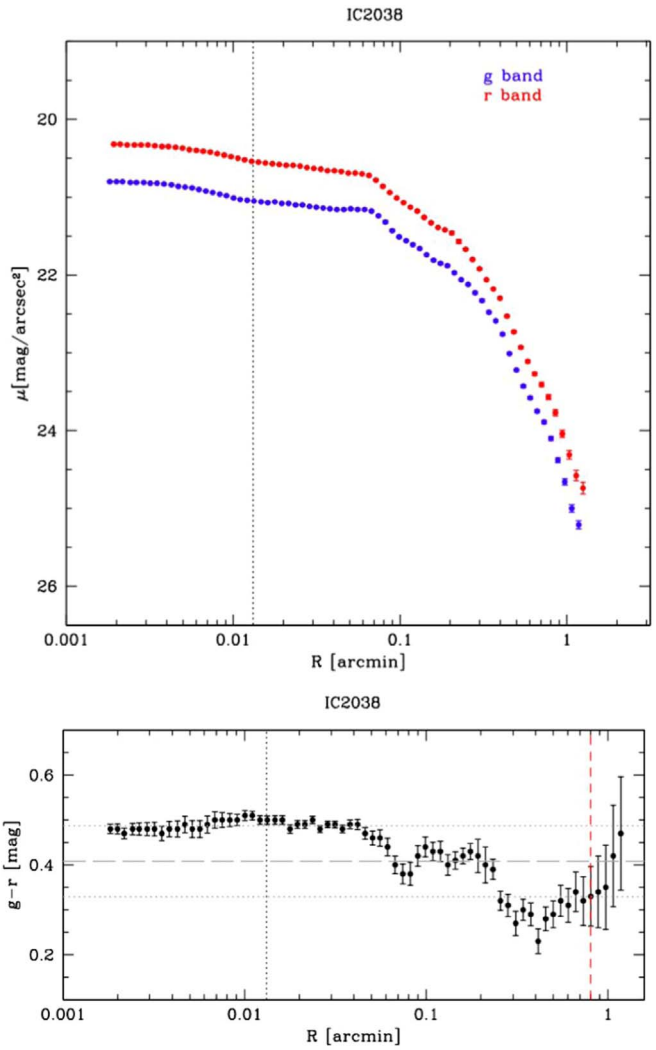

Figure 9. Top panel: azimuthally averaged surface brightness profile as a function of the logarithmic isophote semimajor axis; *g*-band image, blue dots, and *r*-band image, red dots. Bottom panel: azimuthally averaged color profile as a function of the logarithmic isophote semimajor axis. The red dashed vertical line represents the bounds of the region where the mean color value, horizontal dashed gray line, has been estimated.

For NGC 1533, the best fit is made by one Sérsic law and two exponential laws, see Table 6. The first function accounts for the bulge, the inner component; the second one approximate the lens plus the inner disk; and the third models the outer asymmetric envelope (see Figure 11, top middle panel). The stellar envelope starts to dominate the light for $R \geqslant 2'$ ($\sim$6.82 kpc) and has an *r*-band surface brightness in the range 25–29 mag arcsec^{-2} (see Figure 14). The two-dimensional fit is consistent with that obtained on the azimuthally averaged profile (see Tables 6, 4 and 5) and results (model and residuals) are shown in Figure 11. The two-dimensional model (see the middle panel of Figure 11) confirms that the outskirts of NGC 1533 are asymmetric, showing that isophotes are more elongated in the northeast direction. The residual image reports the bar and the spiral-like structure, which has just been revealed by the two-dimensional color map (see Figure 11, top-right panel).

Despite what happens for NGC 1533, in order to have a better estimation of the light distribution between the two interacting galaxies, IC 2038 and IC 2039, and to have a residual image consistent with the system, we contemporary modeled both galaxies in order to take into account the contribution of light of each of them in the overlapping regions (see Figure 11, bottom-middle panel). The light profiles of IC 2038 and IC 2039 are best fitted by a single Sérsic law. The best-fit parameters are reported in Table 6 and the best two-dimensional models are shown in Figure 11 (lower middle panel). In the residual image appears an elongated structure in the direction of NGC 1533−IC 2038 and the light overdensity in the west side of IC 2038 (see Figure 11, lower right panel, and Figure 6).

5. Discussion: Tracing the Build-up History of the NGC 1533 Cloud

In this work we have analyzed the deep VST images, in the *g* and *r* bands, of the Dorado group, centered on the brightest group member NGC 1533. We studied the morphology, light, and color distribution of the galaxy members in the VST fields. The large integration time and the wide field of view of OmegaCAM@VST allow us to map the surface brightness down to $\mu_g \simeq 30.1$ mag arcsec^{-2} and $\mu_r \simeq 28.9$ mag arcsec^{-2} for NGC 1533 ad out 4 R_e, therefore out to regions of the stellar

Table 6
GALFIT Light Profile Decomposition Parameters for g Band

Galaxy	r_e (arcsec)	n	$m_{\rm Srsic}$ (mag)	$r_{0,1}$ (arcsec)	$m_{\rm exp,1}$ (mag)	$r_{0,2}$ (arcsec)	$m_{\rm exp,2}$ (mag)
(1)	(2)	(3)	(4)	(2)	(4)	(2)	(4)
NGC 1533	5.76 ± 0.01	1.70 ± 0.05	12.31 ± 0.06	30.56 ± 0.08	11.31 ± 0.04	180.94 ± 0.3	11.65 ± 0.05
IC 2038	39.61 ± 2.15	1.41 ± 0.07	14.02 ± 0.05	…	…	…	…
IC 2039	11.49 ± 0.58	1.98 ± 0.07	14.43 ± 0.04	…	…	…	…

Note. (1) Galaxy name. Best-fit parameters of the light profile decomposition: (2) effective and scale radius; (3) Sérsic index; (4) integrated magnitude of the different components.

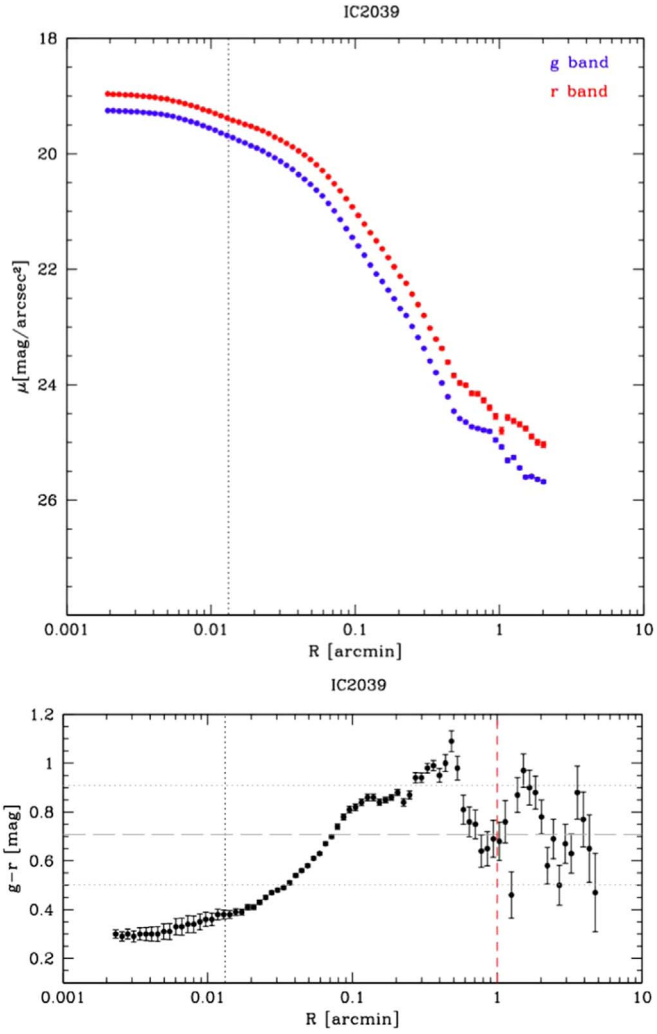

Figure 10. Same as Figure 9 for IC 2039.

halo. The main and new results based on the VST deep imaging are:

1. the optical counterpart of the inner spiral-like features detected in UV by Marino et al. (2011a) with GALEX and by Rampazzo et al. (2017) with *Swift* (see Figure 7);
2. the detection of three faint ($\mu_g \geqslant$ 28–30 mag arcsec^{-2}) spiral-like tails in the north−northwest outskirt of the galaxy (see Figure 6) and an extended (∼5′) arc-like structure with $\mu_g \sim$ 28–30 mag arcsec^{-2}, protruding from the two interacting galaxies, IC 2038 and IC 2039 on the west side;
3. by fitting the extended light profile in the r band, we found that the stellar envelope of NGC 1533 has an exponential profile, it extends out to about 4.′75 (∼16 kpc) and spans the range μ_r = 25–29 mag arcsec^{-2} (see Section 4.3).

In the following sections we discuss the implications from the analysis performed in this work on the building up of the Dorado group of galaxies. In detail, we address the main conclusions on the structure of NGC 1533, from the inner regions to the faint outskirts and on the ongoing interactions between the group members, in turn.

5.1. The Inner Structure of NGC 1533: The Relics of a Past Merger

The 2D $g - r$ color map of NGC 1533 (Figure 5, bottom-right panel) revealed an optical previously undetected arm-like structure in the inner regions, $30'' \leqslant R \leqslant 60''$. The same structure is also evident in the residual image obtained by subtracting the two-dimensional model, obtained from the isophote fit from the original image of NGC 1533 in the g band (see Figure 7). The spiral pattern with redder colors ($g - r \sim 0.8$ mag) on an average bluer ($g - r \sim$ 0.72–0.76 mag) region would resemble a dusty disk. In the same regions, Rampazzo et al. (2017) detected ultraviolet (UV) emissions, which appear as a ring or lens (see also Comerón et al. 2014). Figure 7 shows the residual image of NGC 1533 and the contours levels obtained from the *W2* filter image from *Swift*-UVOT (Rampazzo et al. 2017), where it clearly appears that the ultraviolet arc-like and spots emission regions correspond to the optical arm-like structures. The UV emission detected in the central regions of the galaxy was suggested to be a sign of a recent star formation (Rampazzo et al. 2017). Therefore, this coincidence between the optical and color features detected from VST images and the UV emissions would suggest a merger event that shaped the spiral structure and triggered star formation in the central regions of NGC 1533. Recently Mazzei et al. (2014b) explained the inner structure of NGC 1533 within a major merger; NGC 1533 could arise from a merger between two halos with a mass ratio 2:1 and perpendicular spins. The simulations reproduce the inner ring/arm-like structure visible in the UV bands and the entire spectral energy distribution of the galaxy. In this case, the gas belongs to the merger remnant halo, which could feed the SF. Thom et al. (2012) found that there exist conspicuous gas reservoirs around ETGs, similarly to late types.

5.2. Stellar Halo Component of NGC 1533

In this section we attempt to trace the building-up history of the stellar halo of NGC 1533 by comparing the observed properties with some theoretical predictions. The stellar halos in galaxies are made of stars accreted during the merging events in the form of a "relaxed" component, which is superimposed to

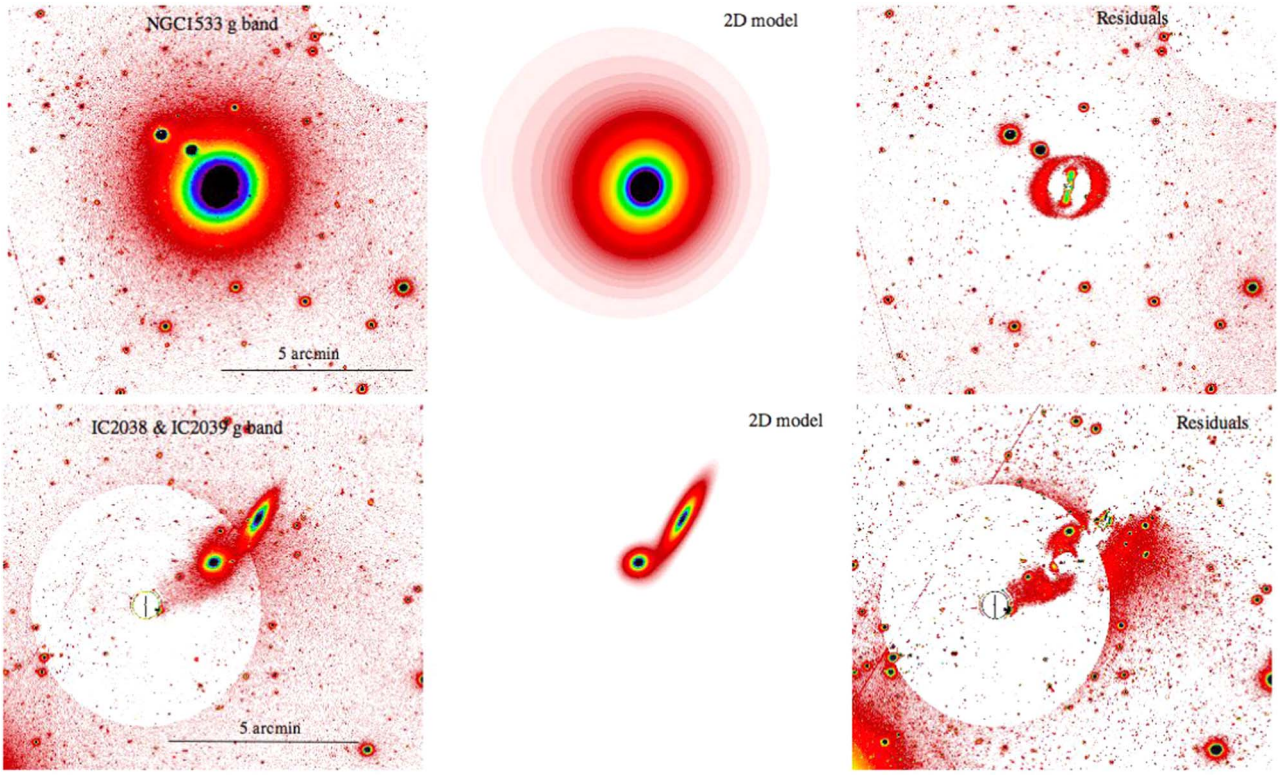

Figure 11. Left panel: *g*-band image, middle panel: best-fit model of the galaxies made with GALFIT, right panel: residual image obtained by subtracting the model from the *g*-band image of NGC 1533 (top panels) and of IC 2038 and IC 2039 (bottom panels).

the stars formed in situ, and the outer and diffuse stellar envelope that is dominated by the "unrelaxed" accreted material (Cooper et al. 2013, 2015). Cosmological simulations of galactic stellar halo formation by the tidal disruption of accreted material are able to give a complete set of "observables" (as structure, density profiles and metallicity) that can be compared with real data. In particular, Cooper et al. (2010) made a detailed analysis of the properties for six simulated stellar halos. They found that the assembly history is made either by a gradual accretion of several progenitors with roughly equal mass or by the accretion of one or two systems. The resulting morphology of the stellar halo is different in the two cases (see Figure 6 in Cooper et al. 2010). The stellar halos built up by the gradual accretion are the most extended, out to 70–100 kpc, and have several streams, shells and other irregular structures, which are more evident at larger radii. On the contrary, the accretion of one or two massive satellites generates smaller stellar halos with a strong central concentration. All features span a surface brightness range 24–35 mag arcsec^{-2} in the *V* band (∼23–35 mag arcsec^{-2} in the *r* band). The shape of the density profile is also different in the two cases, the halos formed by many progenitors are steeper and well fitted by a Sérsic profile with $n \sim 1$, than those formed by few progenitors

The deep VST images for NGC 1533 allow us to map the faint regions of the stellar envelope out to 10′ (∼34.09 kpc). This component starts to dominate the light for $R \geqslant 2'$ (∼6.82 kpc) and has an *r*-band surface brightness in the range 25–29 mag arcsec^{-2} (see Section 4.1). Therefore, at these large distances and surface brightness levels we are able to make a direct comparison between the observed properties and those from theoretical predictions described above.

Table 7
Basic Properties of the Dwarf Galaxies around NGC 1533

Galaxy	R.A. (J2000)	Decl. (J2000)	$m_{\mathrm{tot},g}$ (mag)	$g-r$ (mag)
(1)	(2)	(3)	(4)	(5)
LEDA 75089	$04^{h}11^{m}41\overset{s}{.}0$	$-56^{d}02^{m}55^{s}$	17.4	0.7
LEDA 75054	$04^{h}08^{m}36\overset{s}{.}9$	$-55^{d}48^{m}15^{s}$	18.4	1.1
LEDA 75094	$04^{h}12^{m}05\overset{s}{.}4$	$-55^{d}50^{m}54^{s}$	18	1.2
LEDA 75095	$04^{h}12^{m}15\overset{s}{.}7$	$-55^{d}52^{m}07^{s}$	16.9	0.5

Note. (1) Galaxy name; (2) and (3) J2000 coordinates from NED based on the dwarf galaxies classification made by Ferguson & Sandage (1990); (4) total magnitude in *g* band; (5) mean extinction-corrected color value.

The stellar envelope of NGC 1533 appears quite diffuse and asymmetric, being more elongated toward the northeast (see Figure 6). We have detected three faint tails, one on the north and two others on the west side (see Figure 6 and Section 4.1), which have a surface brightness of ∼28–30 mag arcsec^{-2}. By fitting the azimuthally averaged surface brightness profile of NGC 1533, the outer component, mapping the stellar envelope, is well reproduced by an exponential function (see Section 4.3 and Figure 14). The stellar envelope has a spheroidal form that is highlighted by the variations in P.A. ($90° \leqslant$ P.A. $\leqslant 275°$), ellipticity ($0.025 \leqslant \epsilon \leqslant 0.1$), and color profile (mean color $g - r \simeq 0.46$ mag) in the outer regions. It is rounder than the inner components and twisted (see Figure 13 and the Appendix), and has bluer colors (see Figure 8 and Section 4).

Compared to the simulated halos presented by Cooper et al. (2010), the stellar halo in NGC 1533 has a similar morphology, surface brightness levels, and light distribution to that of the

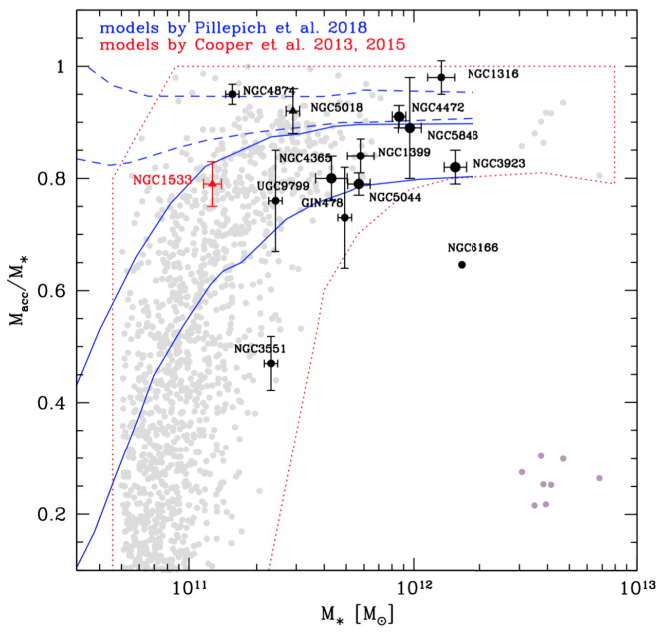

Figure 12. Accreted mass fraction vs. total stellar mass for ETGs. The measurement for NGC 1533 is given as the red triangle. Black circles correspond to other BCGs from the literature (Seigar et al. 2007; Bender et al. 2015; Iodice et al. 2016, 2017b; Spavone et al. 2017b, 2018). The red region indicates the predictions of cosmological galaxy formation simulations by Cooper et al. (2013, 2015). Blue continuous and dashed regions indicate the accreted mass fraction measured within 30 kpc and outside 100 kpc, respectively, in Illustris simulations by Pillepich et al. (2018; see their Figure 12). Purple–gray points show the mass fraction associated with the streams from Table 11 in Cooper et al. (2015).

Aq-A model (shown in Figure 6 of that paper). The Aq-A halo results from the gradual accretion of many progenitors. The stellar mass of the simulated Aq-A galaxy is about $2 \times 10^{10}\,\mathcal{M}_\odot$, which is one order smaller than the stellar mass in NGC 1533 (see Section 4).

It appears with several shells and arc-like tails in the surface brightness range 27–34 mag arcsec^{-2} in the V band, which corresponds to an r-band magnitude of 26–30 mag arcsec^{-2}, fully consistent with the range of surface brightness in the halo of NGC 1533, and is characterized by an exponential light profile, as is also found in NGC 1533.

Further supporting the hypothesis, the outskirts of NGC 1533 formed by the gradual accretion of minor mergers could come by comparing the average colors of these regions with those observed for the dwarf galaxies members of the group. Therefore, from Ferguson & Sandage (1990) we selected the dwarf galaxies in the Dorado group and we derived the mean $g - r$ colors (see Table 7). For all of them, the $g - r \sim 0.88 \pm 0.33$, which is consistent with the average $g - r$ color for the envelope in NGC 1533, i.e., at $R \geqslant 1\farcm5$ (see Figure 8). So, dwarf galaxies of comparable size and luminosity could be considered as small satellites that should be accreted by the NGC 1533 stellar envelope.

As done in Spavone et al. (2017b, 2018), in Figure 12, we compared the total accreted mass fraction estimated for NGC 1533 (see Table 4) with that predicted from theoretical models (Cooper et al. 2013, 2015; Pillepich et al. 2018) and with those derived from observations. We found that the stellar mass fraction of the accreted component derived for NGC 1533 is fully consistent with other BCGs (see Seigar et al. 2007; Bender et al. 2015; Iodice et al. 2016; Spavone et al. 2017b, 2018) and with theoretical models from semi-analytic particle-tagging simulations (Cooper et al. 2013, 2015) and Illustris cosmological hydrodynamical simulations (Pillepich et al. 2018). This further supports the mass assembly history traced above for NGC 1533.

Considering what we have just mentioned and by comparing the morphology and light distribution of this set of simulations with those observed for NGC 1533 (see Section 4.3), we suggest a similar Aq-A model mass assembly history for the stellar halo in this galaxy.

5.3. The Complex Merger History of NGC 1533 System: Who is Interacting with Who?

The analysis of the inner galaxy structure and the stellar envelope, given in the previous sections, suggests that NGC 1533 has a complex history of merging, probably with smaller mass galaxies. The relics of these past interactions still remain in the inner regions of the galaxy and in the outskirts in the form of spiral-like structures and faint tails.

Figure 6 shows the H I emission detected by Ryan-Weber et al. (2003a). To explain the H I gas ring-like formation, Ryan-Weber et al. (2003b) proposed the tidal destruction of a galaxy to form a merger remnant around NGC 1533. Later, by looking at the H I distribution and at the Hα signatures, Ryan-Weber et al. (2004) also suggested that NGC 1533 could be the result of a minor, unequal-mass merger between a gas-rich low surface brightness galaxy and a disk high surface brightness galaxy. The merger transformed the disk galaxy into a barred lenticular galaxy, NGC 1533, and the outer H I disk of low surface brightness galaxy into the giant H I ring around NGC 1533. Moreover Ryan-Weber et al. (2003a) and Bekki et al. (2005) would give reason to the surface brightness levels of the faint features in the galaxy outskirts. According to this simulation, the lack of gas in the inner part of NGC 1533 confirms the hypothesis supported by UV emission and bluer structures that new stars are being generated in the stripped gas, rather than with material at the center of NGC 1533. On the other hand, the H II-confirmed signatures support the hypothesis that new stars are being formed in the giant gas ring (Ryan-Weber et al. 2003a, 2003b; Werk et al. 2010). Looking at the H I velocity dispersion and gradients, the information indicates that stars might have formed by cloud-to-cloud collisions in the H I envelope that is yet to stabilize (Ryan-Weber et al. 2003b).

Tacking into account the H I velocity, one more possible explanation for the elliptical distributions could be that IC 2038, the small late-type galaxy, interacted on a parabolic orbit with NGC 1533 in the past. During the interaction, gas and stars could have been stripped from the outskirts of IC 2038 along the orbit. This would also turn out to be consistent with the presence of the arc-like structure detected on the west side of the group (see Figure 6), which seemed to follow a loop in the direction of NGC 1533. The ATCA H I observations, which are sensitive to an area at least another 5′ to west (compared with the plot A in Figure 1 of Ryan-Weber et al. 2003b), do not show H I emission in this region. It is quite possible that H I is present, but it is below the detection limit.

According to the stellar mass, an estimate of the H I gas content of IC 2038 could be on the order of $\sim 10^9\,\mathcal{M}_\odot$ (Dénes et al. 2014, 2016). The interaction between NGC 1533 and IC 2038 was already proposed by Kilborn et al. (2005) and the

present work put more constraints on it. Nevertheless, IC 2038 does not show unambiguous signatures of interaction, although it seems that it should be an obvious gas donor. Indeed, IC 2039 is an ETG, which are typically gas-poor systems (Young et al. 2018). It is puzzling that our deep imaging suggests that IC 2039 is significantly distorted (residual image from the two-dimensional fit, bottom panel of Figure 11), at odds IC 2038. It has clearly open arms generated by an ongoing interaction, one of which is in the direction of IC 2038 and the other in the opposite direction, suggesting an interaction between them.

6. Concluding Summary

This work represent the first paper of a series aimed to investigate the galaxy evolution in the Dorado group, a still unvirialized galaxy association (Firth et al. 2006) whose bright galaxies show signatures of interaction. In this context, we have obtained new deep images of the field around one of the brightest group members, NGC 1533, as target of the VEGAS Survey. Our deep surface photometry has been motivated by the fact that these galaxies appear embedded into a distorted H I envelope (Kilborn et al. 2005), likely an evolving cloud within the group (Werk et al. 2010; Rampazzo et al. 2017). The present study suggests that NGC 1533 had a complex history made of several interactions with low-mass satellites that generated the star-forming spiral-like structure in the inner regions of the galaxy and are shaping the stellar envelope. In addition, the VST observations show that also the two less-luminous members IC 2038 and IC 2039 are probably interacting each other and, in the past, IC 2038 could have also interacted with NGC 1533, which stripped away gas and stars from its outskirts.

In conclusion, the three Dorado group members (NGC 1533, IC 2038, and IC 2039) may compose an interacting triplet, where the brightest galaxy, NGC 1533, is "red" but not "dead" and with the ongoing mass assembly in the outskirts. Furthermore NGC 1533, IC 2038, and IC 2039 are having a quite eventful life, likely representing one of the "evolving roads" of galaxies in a loose group. The study of both the stellar and ionized gas kinematics will provide important, but still lacking, pieces in composing the puzzle of their co-evolution.

The authors wish to thank the anonymous referee for their comments and suggestions that helped us to improve this paper. The authors are grateful to L. Coccato for his helpful contribution in developing the PSF deconvolution task. A.C., E.I., and M.S. acknowledge financial support from the VST project (P.I. P. Schipani). R.R. and E.V.H. acknowledge funding from the PRIN-INAF eSKApe H I 2017 program 1.05.01.88.04. A.C. thanks E.M. Corsini, E. Sissa, M. Berton, and E. Congiu for useful suggestions. This research has made use of the NASA/IPAC Extragalactic Database (NED), which is operated by the Jet Propulsion Laboratory, California Institute of Technology, under contract with the National Aeronautics and Space Administration. We acknowledge the usage of the HyperLeda database (http://leda.univ-lyon1.fr). IRAF is distributed by the National Optical Astronomy Observatories, which are operated by the Association of Universities for Research in Astronomy, Inc., under cooperative agreement with the National Science Foundation. The VST project is a joint venture between ESO and the National Institute for Astrophysics (INAF) in Naples, Italy.

Facilities: ESO-VST, OmegaCam@ESO-VST.

Software: IRAF, MINUIT, GALFIT, HyperLeda.

Appendix
Isophotal Analysis

A.1. NGC 1533

The analysis of the isophote fit allows us to make the following considerations (see Figure 13): (i) the bulge is located in the region $0\farcs79 < R < 6\farcs95$. It shows a variation in the P.A., 107°–134° < P.A. < 152°, and in ellipticity, $0.033 < \epsilon < 0.102$ and it has roughly zero flat *a4* and *b4* profiles. (ii) The bar plus lens component is located in the range $6\farcs95 < R < 46\farcs7$. It has a variation in the P.A., 152° < P.A. < 166° for $6\farcs95 < R < 29''$ and 102° < P.A. < 166° for $29'' < R < 46\farcs7$. The ellipticity increases, $0.102 < \epsilon < 0.369$, for $6\farcs95 < R < 29''$ then decreases, $0.055 < \epsilon < 0.365$, for $29'' < R < 46\farcs7$. (iii) The outer ring lens structure is located in the region $46\farcs7 < R < 82\farcs58$; it has a variation in the P.A., 108° < P.A. < 122°, and in ellipticity, $0.055 < \epsilon < 0.085$, and it has maximum values ∼0.005 and ∼0.01 of *a4* and *b4*, respectively. (iv) The disk plus stellar envelope component is located out of $R > 82\farcs58$.

Based on the isophotal analysis, the azimuthally averaged surface brightness profile is best reproduced by a multi-component model; the profile is fitted with three components: two Sérsic and an outer exponential function. These three elements define the different light components dominating the galaxy light distribution at different scales (Figure 14 and Table 4).

A.2. IC 2038

The geometrical parameters of IC 2038 confirm that the galaxy is a late-type (Figure 13). The P.A. is approximately constant around ∼145°–155°, while the ellipticity has a rapid increase, from 0.2 to 0.7, in the central regions, between $0\farcs79$ and $4\farcs2$, and then sets in a range of ∼0.6–0.8 outside $12''$. This behavior highlights a disky nature that is confirmed by the positive values, in all galaxy extensions, of the *b4* profile. The large error bars of these two last parameters are compliant with the presence of dust.

The azimuthally averaged surface brightness profile is best reproduced by a multi-component model: the profile is fitted with a Sérsic and an outer exponential function, as shown in Figure 14 and Table 5.

A.3. IC 2039

Looking at Figure 13 (bottom panels), IC 2039 presents an ellipticity lower than ∼0.25 up to $42''$ and a constant increase to ∼0.8 at about $2'$. On the contrary, the P.A. has a first roughly linear increasing trend, ∼100°–125°, inside $18''$ and then it scatters from 100° to 150°. The complexity of the structure is consistent with the *a4* and *b4* profiles. In particular, *b*4 shows a inner flat component, supposedly the bulge, a positive trend between $4\farcs8 \leqslant R \leqslant 24''$, probably due to a disky component. We reproduced the azimuthally averaged surface brightness profile using a Sérsic and an exponential function. These two elements should define the bulge light component and an outer disk feature (Figure 14 and Table 5).

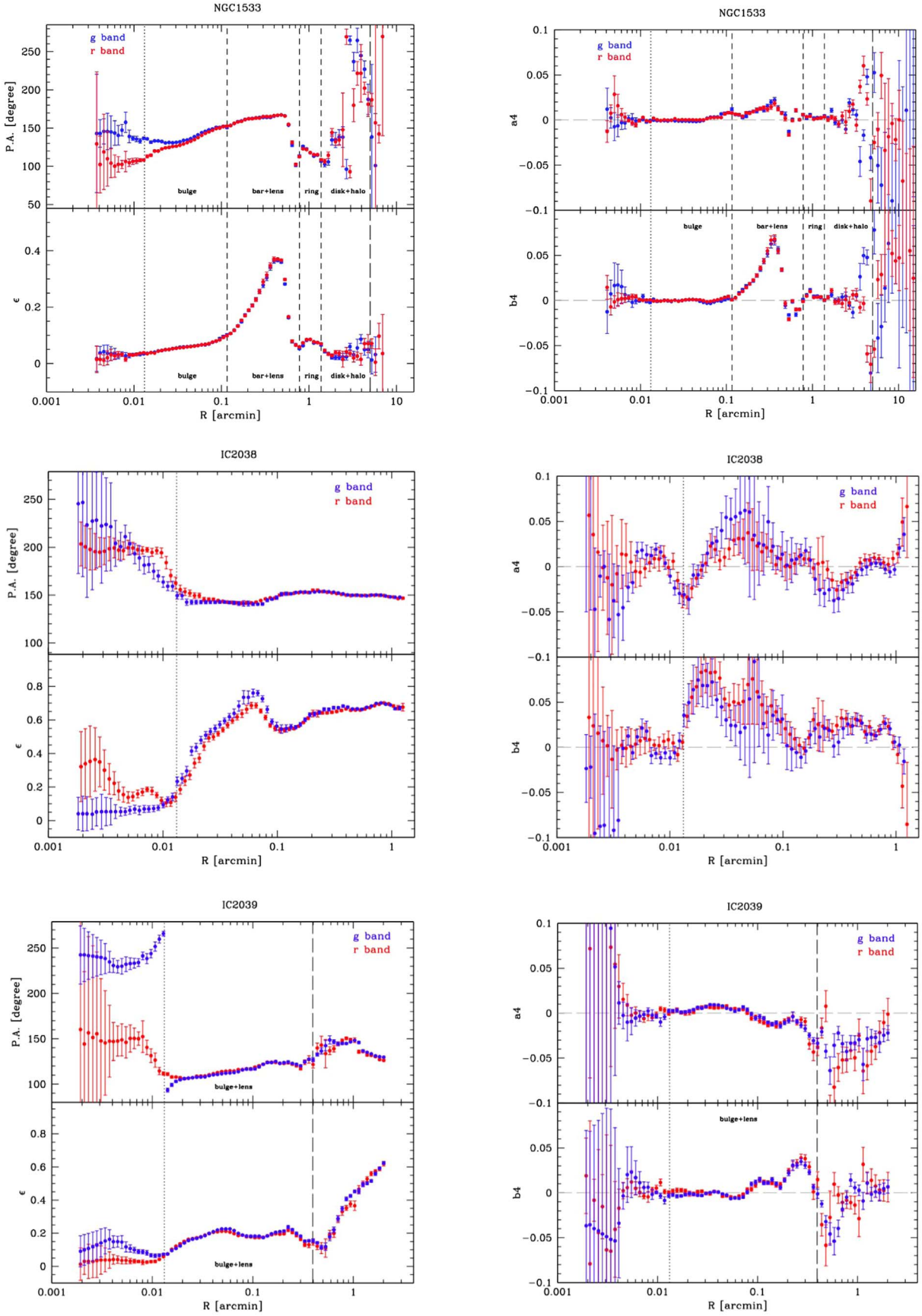

Figure 13. Position angle (top-left panel), ellipticity (bottom-left panel), $a4$ (top-right panel), and $b4$ (bottom-right panel) profiles plotted against the isophote semimajor axis. These plots are obtained with ELLIPSE from the g-band image, blue dots, and r-band image, red dots.

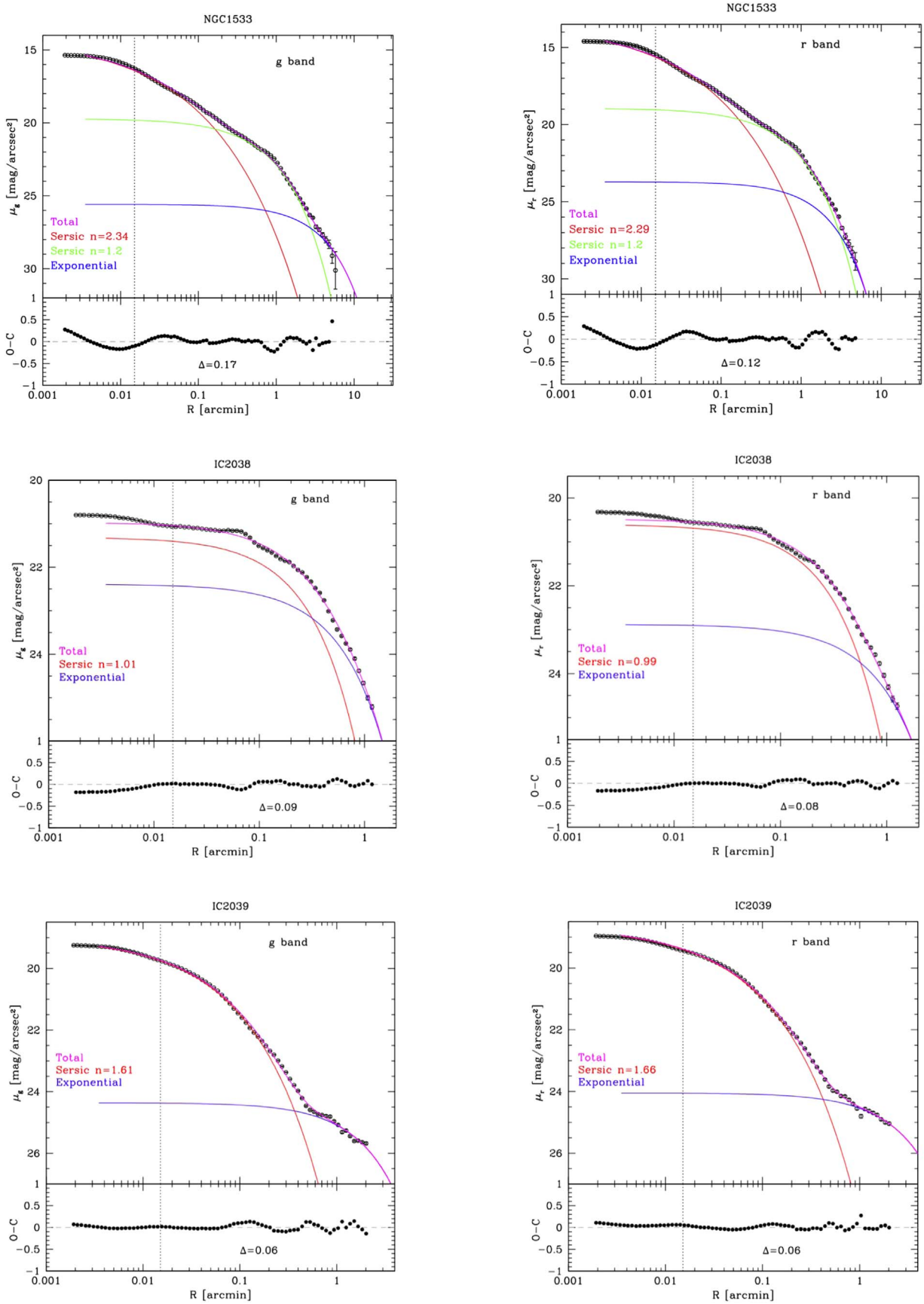

Figure 14. Azimuthally averaged (and PSF deconvolved for NGC 1533) surface brightness profiles in the *g* band (left panels) and in *r* band (right panels) and the residuals between the observed surface brightness and the best fit; the gray dashed line indicates the zero level. Top panels refer to NGC 1533, middle panels to IC 2038, and bottom panels to IC 2039. Red and green solid lines represent Sérsic laws, blue solid line represent exponential function, and the magenta solid line is the resulting best-fit interpolation. The vertical dotted line delimits the regions affected by seeing, which are excluded from the fit.

ORCID iDs

Arianna Cattapan https://orcid.org/0000-0002-5172-3108
Marilena Spavone https://orcid.org/0000-0002-6427-7039
Enrichetta Iodice https://orcid.org/0000-0003-4291-0005
Stefano Ciroi https://orcid.org/0000-0001-9539-3940
Pietro Schipani https://orcid.org/0000-0003-0197-589X
Aniello Grado https://orcid.org/0000-0002-0501-8256
Luca Limatola https://orcid.org/0000-0002-1896-8605

References

Arnaboldi, M., Ventimiglia, G., Iodice, E., Gerhard, O., & Coccato, L. 2012, A&A, 545, A37
Arp, H. C., & Madore, B. F. 1987, A Catalogue of Southern Peculiar Galaxies and Associations (Cambridge: Cambridge Univ. Press)
Bekki, K., Koribalski, B. S., Ryder, S. D., & Couch, W. J. 2005, MNRAS, 357, L21
Bender, R., Kormendy, J., Cornell, M. E., et al. 2015, ApJ, 807, 56
Boselli, A., & Gavazzi, G. 2014, A&ARv, 22, 74
Bressan, A., Panuzzo, P., Buson, L., et al. 2006, ApJL, 639, L55
Brough, S., Forbes, D. A., Kilborn, V. A., & Couch, W. 2006, MNRAS, 370, 1223
Cantiello, M., D'Abrusco, R., Spavone, M., et al. 2018, A&A, 611, A93
Caon, N., Capaccioli, M., & D'Onofrio, M. 1993, MNRAS, 265, 1013
Capaccioli, M., Spavone, M., Grado, A., et al. 2015, A&A, 581, A10
Carrasco, E. R., Mendes de Oliveira, C., Infante, L., & Bolte, M. 2001, AJ, 121, 148
Cattapan, A., Iodice, E., & Rampazzo, R. 2018, A Deep Look at NGC1533 in the Dorado Group with VST, Zenodo, doi:10.5281/zenodo.1303938
Clemens, M. S., Bressan, A., Nikolic, B., et al. 2006, MNRAS, 370, 702
Clemens, M. S., Bressan, A., Nikolic, B., & Rampazzo, R. 2009, MNRAS, 392, L35
Comerón, S., Salo, H., Laurikainen, E., et al. 2014, A&A, 562, A121
Cooper, A. P., Cole, S., Frenk, C. S., et al. 2010, MNRAS, 406, 744
Cooper, A. P., D'Souza, R., Kauffmann, G., et al. 2013, MNRAS, 434, 3348
Cooper, A. P., Gao, L., Guo, Q., et al. 2015, MNRAS, 451, 2703
D'Abrusco, R., Cantiello, M., Paolillo, M., et al. 2016, ApJL, 819, L31
de Jong, R. S. 2008, MNRAS, 388, 1521
de Vaucouleurs, G. 1975, in Stars and Stellar Systems, Vol. 9, ed. A. Sandage, M Sandage, & J. Kristian (Chicago, IL: Univ. Chicago Press), 557
Dénes, H., Kilborn, V. A., & Koribalski, B. S. 2014, MNRAS, 444, 667
Dénes, H., Kilborn, V. A., Koribalski, B. S., et al. 2016, MNRAS, 455, 1294
Donzelli, C. J., Muriel, H., & Madrid, J. P. 2011, ApJS, 195, 15
Duc, P.-A., Cuillandre, J.-C., Karabal, E., et al. 2015, MNRAS, 446, 120
Eales, S., de Vis, P., Smith, M. W. L., et al. 2017, MNRAS, 465, 3125
Fall, S. M., & Efstathiou, G. 1980, MNRAS, 193, 189
Ferguson, H. C., & Sandage, A. 1990, AJ, 100, 1
Ferrarese, L., Côté, P., Cuillandre, J.-C., et al. 2012, ApJS, 200, 4
Firth, P., Evstigneeva, E. A., Jones, J. B., et al. 2006, MNRAS, 372, 1856
Freeman, K. C. 1970, ApJ, 160, 811
Grado, A., Capaccioli, M., Limatola, L., & Getman, F. 2012, MSAIS, 19, 362
Houck, J. R., Roellig, T. L., van Cleve, J., et al. 2004, ApJS, 154, 18
Huang, S., Ho, L. C., Peng, C. Y., Li, Z.-Y., & Barth, A. J. 2013, ApJ, 766, 47
Iodice, E., Arnaboldi, M., Rejkuba, M., et al. 2014, A&A, 567, A86
Iodice, E., Capaccioli, M., Grado, A., et al. 2016, ApJ, 820, 42
Iodice, E., Spavone, M., Cantiello, M., et al. 2017a, ApJ, 851, 75
Iodice, E., Spavone, M., Capaccioli, M., et al. 2017b, ApJ, 839, 21
Iodice, E., Spavone, M., Capaccioli, M., et al. 2019, A&A, 623, A1
Jedrzejewski, R. I. 1987, MNRAS, 226, 747
Jeong, H., Yi, S. K., Bureau, M., et al. 2009, MNRAS, 398, 2028
Kaneda, H., Onaka, T., & Sakon, I. 2005, ApJL, 632, L83
Karachentsev, I. D., Makarov, D. I., & Kaisina, E. I. 2013, AJ, 145, 101
Kilborn, V. A., Koribalski, B. S., Forbes, D. A., Barnes, D. G., & Musgrave, R. C. 2005, MNRAS, 356, 77
La Barbera, F., Ferreras, I., de Carvalho, R. R., et al. 2012, MNRAS, 426, 2300
Lucy, L. B. 1974, AJ, 79, 745
Malin, D. F., & Carter, D. 1983, ApJ, 274, 534
Marino, A., Bianchi, L., Rampazzo, R., et al. 2011a, ApJ, 736, 154
Marino, A., Mazzei, P., Rampazzo, R., & Bianchi, L. 2016, MNRAS, 459, 2212
Marino, A., Rampazzo, R., Bianchi, L., et al. 2011b, MNRAS, 411, 311
Mazzei, P., Marino, A., & Rampazzo, R. 2014a, ApJ, 782, 53
Mazzei, P., Marino, A., Rampazzo, R., et al. 2018a, A&A, 610, A8
Mazzei, P., Marino, A., Rampazzo, R., Galletta, G., & Bettoni, D. 2014b, AdSpR, 53, 950
Mazzei, R., Vijayaraghavan, R., & Sarazin, C. L. 2018b, AAS Meeting, 231, 252.12
Merritt, A., van Dokkum, P., Abraham, R., et al. 2016, ApJ, 830, 62
Michard, R. 2002, A&A, 384, 763
Mihos, J. C., Harding, P., Feldmeier, J. J., et al. 2017, ApJ, 834, 16
Morrissey, P., Conrow, T., Barlow, T. A., et al. 2007, ApJS, 173, 682
Muñoz, R. P., Eigenthaler, P., Puzia, T. H., et al. 2015, ApJL, 813, L15
Oemler, A., Jr., Abramson, L. E., Gladders, M. D., et al. 2017, ApJ, 844, 45
Panuzzo, P., Rampazzo, R., Bressan, A., et al. 2011, A&A, 528, A10
Peng, C. Y., Ho, L. C., Impey, C. D., & Rix, H.-W. 2002, AJ, 124, 266
Peng, C. Y., Ho, L. C., Impey, C. D., & Rix, H.-W. 2010, AJ, 139, 2097
Pillepich, A., Nelson, D., Hernquist, L., et al. 2018, MNRAS, 475, 648
Pohlen, M., & Trujillo, I. 2006, A&A, 454, 759
Rampazzo, R., Marino, A., Tantalo, R., et al. 2007, MNRAS, 381, 245
Rampazzo, R., Mazzei, P., Marino, A., et al. 2017, A&A, 602, A97
Rampazzo, R., Mazzei, P., & Marino, A. 2018, In the Shade of Dorado Group Giants: Tracing the Eventful Life of Member Galaxies in Optical and Far UV, Zenodo, doi:10.5281/zenodo.1304773
Rampazzo, R., Panuzzo, P., Vega, O., et al. 2013, MNRAS, 432, 374
Ricciardelli, E., Vazdekis, A., Cenarro, A. J., et al. 2012, MNRAS, 424, 172
Richardson, W. H. 1972, JOSA, 62, 55
Rodríguez, S., Padilla, N. D., & García Lambas, D. 2016, MNRAS, 456, 571
Ryan-Weber, E., Webster, R., & Bekki, K. 2003a, ASSL, 281, 223
Ryan-Weber, E. V., Meurer, G. R., Freeman, K. C., et al. 2004, AJ, 127, 1431
Ryan-Weber, E. V., Webster, R. L., & Staveley-Smith, L. 2003b, MNRAS, 343, 1195
Salim, S., & Rich, R. M. 2010, ApJL, 714, L290
Schlafly, E. F., & Finkbeiner, D. P. 2011, ApJ, 737, 103
Seigar, M. S., Graham, A. W., & Jerjen, H. 2007, MNRAS, 378, 1575
Sérsic, J. L. 1963, BAAA, 6, 41
Spavone, M., Capaccioli, M., Napolitano, N. R., et al. 2017a, Msngr, 170, 34
Spavone, M., Capaccioli, M., Napolitano, N. R., et al. 2017b, A&A, 603, A38
Spavone, M., Iodice, E., Capaccioli, M., et al. 2018, ApJ, 864, 149
Strateva, I., Ivezić, Ž., Knapp, G. R., et al. 2001, AJ, 122, 1861
Thilker, D. A. 2008, ASSP, 5, 109
Thom, C., Tumlinson, J., Werk, J. K., et al. 2012, ApJL, 758, L41
Trujillo, I., & Fliri, J. 2016, ApJ, 823, 123
Tully, R. B. 2015, AJ, 149, 171
Tully, R. B., Courtois, H. M., Dolphin, A. E., et al. 2013, AJ, 146, 86
van Dokkum, P. G., Abraham, R., & Merritt, A. 2014, ApJL, 782, L24
Vazdekis, A., Ricciardelli, E., Cenarro, A. J., et al. 2012, MNRAS, 424, 157
Vega, O., Bressan, A., Panuzzo, P., et al. 2010, ApJ, 721, 1090
Weigel, A. K., Schawinski, K., Caplar, N., et al. 2017, ApJ, 845, 145
Werk, J. K., Putman, M. E., Meurer, G. R., et al. 2008, ApJ, 678, 888
Werk, J. K., Putman, M. E., Meurer, G. R., et al. 2010, AJ, 139, 279
Werner, M. W., Uchida, K. I., Sellgren, K., et al. 2004, ApJS, 154, 309
Wyder, T. K., Martin, D. C., Schiminovich, D., et al. 2007, ApJS, 173, 293
Young, L. M., Serra, P., Krajnović, D., et al. 2018, MNRAS, 477, 2741
Zackrisson, E., Bergvall, N., Östlin, G., et al. 2006, ApJ, 650, 812